REPORT

Direct observation of charge density and electronic polarization in fluorite ferroelectrics by 4D-STEM

Shiyu Wang,[1,2] Xinyan Li,[1,3] Yunzhe Jia,[1,2] Hao Xiong,[4] Ting Lin,[1,2] Pengxiang Ji,[1,2] Tongtong Shang,[5] Hai Zhong,[1,6] Xiao Chen,[4] Chen Ge,[1,2] Sheng Meng,[1,2,7] Qinghua Zhang,[1,*] and Lin Gu[5,*]

*Correspondence: lingu@tsinghua.edu.cn (L.G.); zqh@iphy.ac.cn (Q.Z.)

Received: November 21, 2023; Accepted: April 25, 2024; Published Online: May 11, 2024; https://doi.org/10.59717/j.xinn-mater.2024.100068

GRAPHICAL ABSTRACT

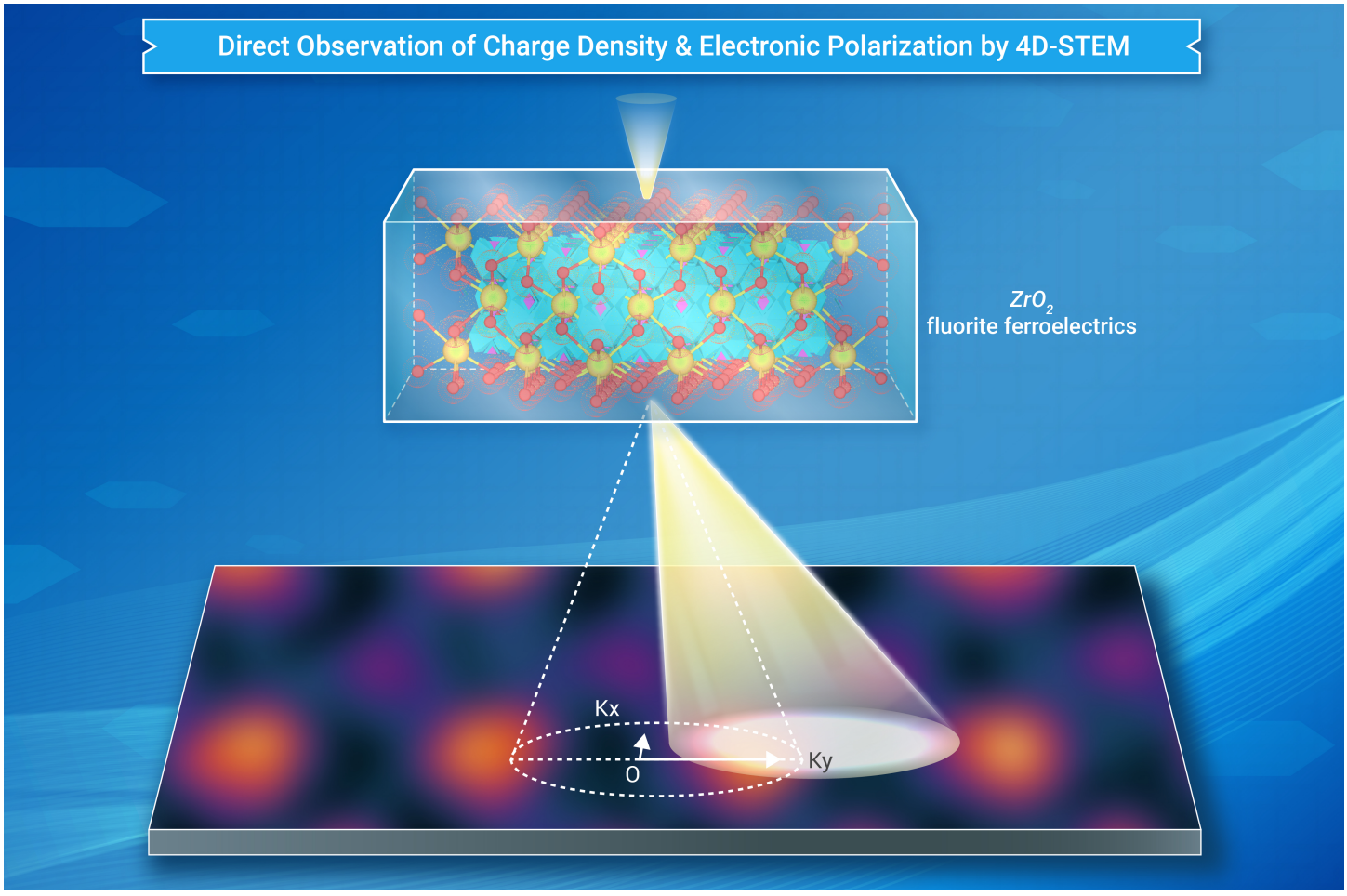

PUBLIC SUMMARY

- The real-space charge density of the ZrO_2 with sub-Ångström resolution is observed.
- The electronic contribution to the total spontaneous polarization is non-negligible.
- The local polarization suggests a gradual increase in the covalent nature of the Zr-O bond.

REPORT

Direct observation of charge density and electronic polarization in fluorite ferroelectrics by 4D-STEM

Shiyu Wang,[1,2] Xinyan Li,[1,3] Yunzhe Jia,[1,2] Hao Xiong,[4] Ting Lin,[1,2] Pengxiang Ji,[1,2] Tongtong Shang,[5] Hai Zhong,[1,6] Xiao Chen,[4] Chen Ge,[1,2] Sheng Meng,[1,2,7] Qinghua Zhang,[1,*] and Lin Gu[5,*]

[1]Beijing National Laboratory for Condensed Matter Physics, Institute of Physics, Chinese Academy of Sciences, Beijing 100190, China
[2]School of Physical Sciences, University of Chinese Academy of Science, Beijing 100049, China
[3]College of Materials Science and Opto-Electronic Technology, University of Chinese Academy of Sciences, Beijing 100049, China
[4]Beijing Key Laboratory of Green Chemical Reaction Engineering and Technology, Department of Chemical Engineering, Tsinghua University, Beijing 100084, China
[5]Beijing National Center for Electron Microscopy & Laboratory of Advanced Materials, Department of Materials Science & Engineering, Tsinghua University, Beijing 100084, China
[6]School of Physics and Optoelectronic Engineering, Ludong University, Yantai 264025, China
[7]Songshan Lake Materials Laboratory, Dongguan 523808, China
*Correspondence: lingu@tsinghua.edu.cn (L.G.); zqh@iphy.ac.cn (Q.Z.)

Received: November 21, 2023; Accepted: April 25, 2024; Published Online: May 11, 2024; https://doi.org/10.59717/j.xinn-mater.2024.100068

Citation: Wang S., Li X., Jia Y., et al., (2024). Direct observation of charge density and electronic polarization in fluorite ferroelectrics by 4D-STEM. The Innovation Materials **2(2)**: 100068.

The fluorite ferroelectrics is extremely promising for memory applications due to the silicon compatibility and the robust ferroelectricity with decreasing size. However, the direct observation of local electronic polarization remains elusive, thereby hindering the comprehension of the atomic-scale origin of ferroelectricity. Here, we directly map the real-space charge density of the ZrO_2 nanocrystal in its polar, nonpolar, as well as interphase regions with sub-Ångström resolution by four-dimensional scanning transmission electron microscopy (4D-STEM). Based on the variation of the electric dipole moments, we analyze the electronic contribution to the total spontaneous polarization, which reaches a maximum of 17.8%. In comparison to the continuous polarization in conventional ferroelectric units, the local polarization profile looks like a maple leaf edge at the tetragonal-orthorhombic phase interface, which suggests a gradual increase in the electronic polarization and the covalent nature of the Zr-O bond. We validate these findings with 4D-STEM simulations and calculations based on density functional theory. These findings provide atomic insights into the bonding nature and phase transition feature in fluorite oxides, and unravel the likely origin of ferroelectricity in ferroelectrics.

INTRODUCTION

Ferroelectric (FE) materials have been extensively studied since first discovery in the early 1920s,[1] which are spontaneously polarized and can experience polarization switching under an external electric field. By contrast, antiferroelectric (AFE) materials are characterized by the alignment of equal but antiparallel adjacent dipole moment rows, thus exhibiting zero macroscopic polarization. They can undergo field-induced reversible transitions between FE and AFE phases.[2,3] In some conventional perovskite-type FE materials, such as $BiFeO_3$ and $BaTiO_3$, the spontaneous polarization is mainly attributed to the displacements of ions from the crystal structure analysis.[4,5] However, previous studies have shown that in some specific FE materials, such as $KNbO_3$ and $PbTiO_3$, polarization values cannot be interpreted merely according to the simple ionic polarization model,[6,7] in which case the electronic polarization plays a significant role in determining the related ferroelectric properties.

The zirconium oxide (ZrO_2) has attracted considerable attention since the discovery of unconventional ferroelectricity and antiferroelectricity in the ZrO_2-based thin films.[8–11] These materials are highly promising for future high-density, low-power memory device applications due to the compatibility with complementary metal-oxide-semiconductor (CMOS) processing and the robust ferroelectricity even in films thinner than 10 nm. It has been proved that the ferroelectricity is originated from the polar orthorhombic phase (O-phase) with space group $Pca2_1$ that lacks an inversion center.[8,12] The FE phase is formed via phase transition from the nonpolar $P4_2/nmc$ tetragonal crystalline structure, which is affected by several thermodynamic and kinetic factors.[13] However, the true ferroelectric nature of pure ZrO_2 thin films and its origin at a microscopic level remain unclear. Previous studies indicate that electronic polarization may be a significant contributor to the origin of ferroelectricity, which requires further investigation.[14,15] Therefore, it is critical to identify the local electronic polarization at atomic resolution, which contains different information compared to the bulk material phases.

There are various metastable polymorphs of fluorite oxides in nanoscale thin films, including monoclinic (M), tetragonal (T), and ferroelectric orthorhombic (O) phases.[16,17] In view of this, the various interphases play a key role in understanding the relationship between crystalline structure and ferroelectric properties of fluorite oxides. Therefore, a few experimental and theoretical works have been devoted to the microscopic interface structure.[18–21] The presence of interphase boundaries is expected to affect the phase stability due to differences in local epitaxial strain or departures from the monoclinic and orthorhombic lattices.

However, atomic-scale direct observation of local charge density distribution near the interphase of ferroelectric fluorite oxides remains limited, mainly restricted by the lack of proper characterization method with high resolution.

Recently, four-dimensional scanning transmission electron microscopy (4D-STEM) has provided the ability to image the charge density map at the atomic scale,[22,23] by focusing the electron probe onto the sample surface and collecting two-dimensional (2D) diffraction patterns over a 2D grid of probe positions.[24] Since then, much progress has been made in imaging local electron distributions in real space. For example, Fang et al. used 4D-STEM to map the charge density around line defects in MoS_2 and WS_2, successfully locating electron-rich regions of 1D conduction channels in line vacancies.[23] Gao et al. revealed the charge density at the interface of $SrTiO_3$ and $BiFeO_3$ in real space with sub- Ångström resolution by 4D-STEM,[22] further confirming the powerful potentials of this method to probe local bonding in heterogeneous materials.

In this article, we perform real-space charge imaging on nanocrystalline ZrO_2 by 4D-STEM, which can obtain local charge density maps in the T and O phases and near the transitional phase interface, allowing atomic scale investigations of the bulk and interface structure between polar and nonpolar phases and charge density redistribution in the same ZrO_2 nanocrystals. We demonstrate the deformed shapes of electric field and charge density around O columns in the polar and nonpolar phase interface. Meanwhile, the differences between total spontaneous polarization and ionic polarization are directly visualized and clarified. In contrast to the continuous polarization in conventional ferroelectric units, the local polarization profile looks like a maple leaf edge at the tetragonal-orthorhombic (T-O) phase interface, indicating the gradually increasing electronic polarization and the stronger covalent nature of the Zr-O bonds. The results indicate that the hybridization between O and Zr orbitals is crucial for the considerable spontaneous polarization. These findings unravel the microscopic phase interface structure in nanoscale fluorite oxides, providing a new insight for investigating the microscopic mechanism behind the origin of ferroelectricity in fluorite-structure ferroelectrics.

MATERIALS AND METHODS

Materials and sample preparation

ZrO_2 thin films and a $La_{0.8}Sr_{0.2}MnO_3$ (LSMO) buffer layer were grown by pulsed laser deposition (PLD) method on $SrTiO_3$ (001) substrate. A XeCl excimer laser with 308nm wavelength was used and the imaged laser spot was 4.0 mm^2. The growth of the LSMO layer and ZrO_2 layer was both carried out at 780°C with 1.25 J cm^{-2} laser fluence at a repetition rate of 2 Hz. The dynamic oxygen pressure is controlled under 25 Pa and 13 Pa, respectively. After deposition, the heterostructure was in situ annealed at 650°C under a 10 kPa oxygen pressure for 10 min and then cooled down to room temperature at a rate of 10 °C min^{-1}. The ZrO_2 thin film in O-phase is kinetically stabilized by surface and grain boundary energies.

We directly transferred the ZrO_2 film to a transmission electron microscopy (TEM) Cu grid for plan-view imaging to minimize the thickness of TEM specimen and obtain better contrast in 4D-STEM imaging. After growth, the sample was immersed in KI + HCl + H_2O solution for etching LSMO. After several hours, the unclamped thin films were then removed from the substrate by slowly dipping the substrate in deionized water. Finally, the released film was picked up by a TEM Cu grid for subsequent plan-view TEM characterization and then dried up on a hot plate at 95°C.

Measurement of specimen thickness

Position-averaged CBED (PACBED) is carried out by acquiring the average CBED pattern in the diffraction plane while the electron beam scans across a small area. A smaller convergence angle of approximately 12.3 mrad is used. To quantitatively determine the thickness of our samples, we compare the experimental results with simulated PACBED patterns. The database of simulated PACBED patterns is generated using multislice simulation containing PACBED patterns from different sample thicknesses at the same imaging condition (300 kV, 12.3 mrad). The sample thickness is then estimated at the precision of around 1 nm. The experimental PACBED in Figure S1 B is taken experimentally from the boxed area of ZrO_2 labelled in the HAADF-STEM image. This PACBED is compared with simulated PACBEDs from samples of thickness 1–19 nm. Quantitatively, a least-squares fitting is carried out on PACBEDs, showing that the ZrO_2 region is approximately 5 nm thick. The fitting result is consistent with the thickness measured from the cross section in Figure S1 A.

4D-STEM Measurement

Scanning transmission electron microscopy was performed using a Cs-corrected STEM (FEI Titan Cubed Themis G2 300), operated at an accelerating voltage of 300 kV. This STEM is equipped with a DCOR+ spherical aberration corrector for the electron probe, which was aligned with proper aberration coefficients using a standard gold sample. The convergence semi-angle is 23 mrad and the beam current is 20 pA; Each 4D-STEM dataset contains 128 × 128 CBED patterns and the dwell time in each CBED pattern (equals to a pixel in the final image) is 1 ms. The ultrafast 2D pixelated detector used for the 4D-STEM work is the EMPAD, which combines direct electron detection with rapid pixelated readout for dynamic imaging. The obtained images are applied with Gaussian filter to denoise and smooth (Figure S12). Unit cell averaging was used to improve the data quality (Figure S13). This was achieved in three steps: (1) Atom positions were identified in the electrostatic potential image using AtomSegNet,[25] a deep-learning model for high-precision atom localization. (2) Atoms were classified into Zr and O based on the simultaneously acquired HAADF-STEM image intensity. (3) Some Zr atom positions away from defect sites and contaminants were selected. unit cell averaging was carried out at these atom sites in the CoM, phase and charge density images to yield high quality images.

Data processing

Codes written in Python were used to process the entire 4D-STEM dataset. The HAADF are reconstructed from the 4D dataset by integrating the intensity of the annular regions of 32–64 mrad from the CBED patterns. As shown in the reference,[26] the x and y components of the COM of the diffraction pattern, *Icomx* and *Icomy*, are proportional to the electric field components *Ex* and *Ey*, respectively. Thus, the direction of the electric field vector $\vec{E}_\perp$ can be calculated by:

$$\vec{E}_\perp = E_x\vec{i} + E_y\vec{j}$$

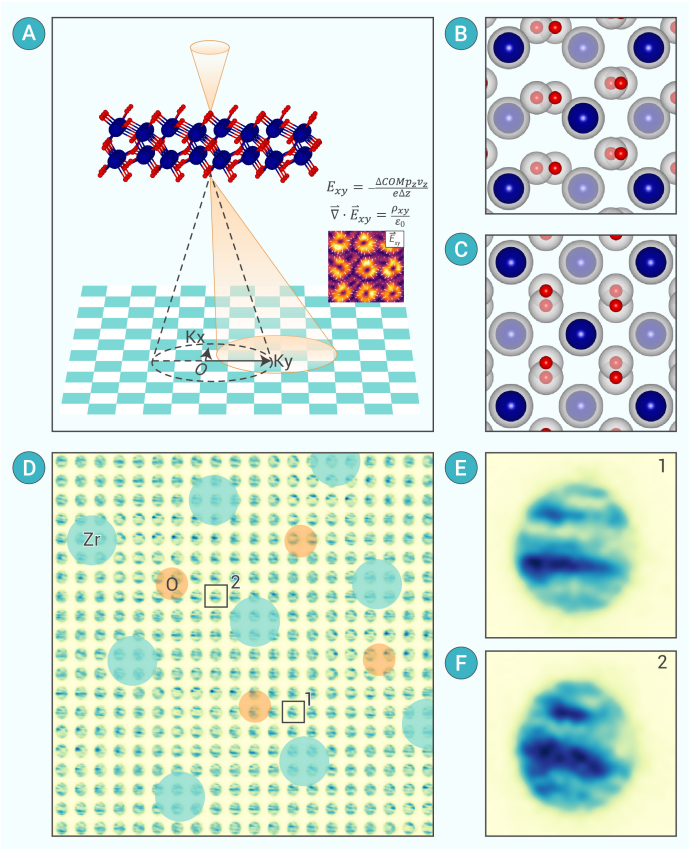

Figure 1. Experimental setup and main principles (A) Schematic of the calculation of the COM at each point of the electron probe and the derivation of the electric field map from the COM. (B)-(C) Atomic structure of ZrO_2 in the (B) ferroelectric O phase and (C) nonpolar T phase along the [100] projection direction, obtained from DFT calculations. Zr atoms are in blue and O in red. The gray circles represent the electron density around the nuclei. (D) 4D-STEM data plotted as montage of CBED patterns, showing variations as a function of probe position relative to Zr and O atom positions. (E)-(F) CBED patterns from the positions marked with the black box 1 (E) and 2 (F).

As demonstrated in the reference,[22] the magnitude of $|\vec{E}_\perp|$ is proportional to the shift in the COM from the geometric centre, ΔCOM:

$$E_\perp = -\frac{\Delta COM p_z v_z}{e''\Delta z}$$

Where p_z and v_z are the momentum and velocity of the electron beam along the beam direction respectively, e is the elementary charge constant and Δz is the sample thickness. The charge density (ρ) in units of $e/Å^2$ was calculated according to Gauss's law:

$$\rho = \varepsilon_0 \nabla \cdot E_\perp$$

where ε_0 is the vacuum permittivity. The colormaps of the resulting images have been appropriately chosen to highlight the locations of the O atom columns.

As shown in Figure S10, ΔCOM is simulated for different thicknesses in comparison with the electric field calculated from DFT (E_{DFT}). To simplify the comparison, the electric fields are scaled and multiplied by Δz to be dimensionless. For sample thickness below 5.5 nm, the measured ΔCOM is directly proportional to E_{DFT}. However, ΔCOM starts to deviate from the values expected from E_{DFT} for 6nm sample thickness. In summary, for thicknesses below 5.5 nm, the linearity approximation appears to be sufficiently accurate allowing the direct electric field measurement from the shift of COM. For samples thicker than 6 nm, the accuracy gradually falls off.

DFT calculation

Pseudo-potential DFT calculation of electronic structure is implemented via Vienna Ab initio Simulation Package (VASP) and the post-processing of orbital projection is completed with the help of vaspkit package. Calculation is

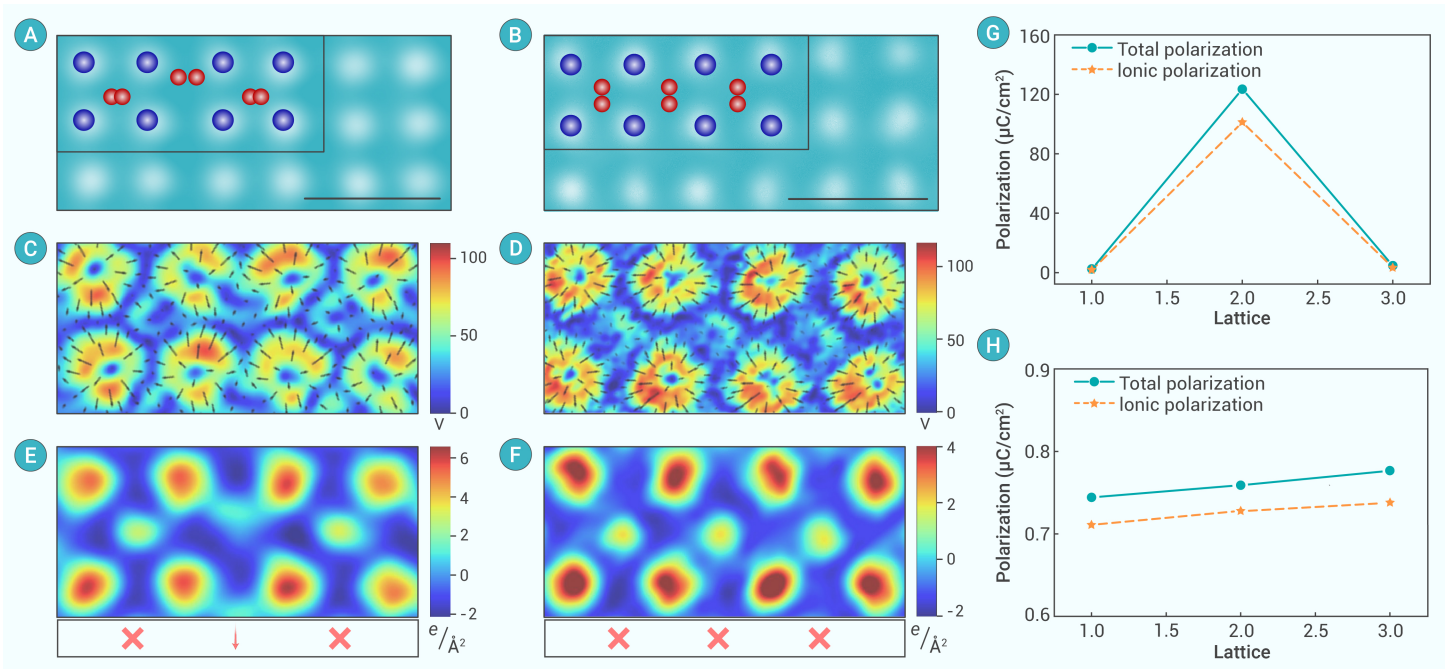

Figure 2. Real-space charge-density mapping and polar analysis in orthorhombic and tetragonal ZrO_2 (A)-(B) Atomic-resolved HAADF images of ferroelectric O-phase (A) and nonpolar T-phase (B) taken from the [100] zone axis. Zr atoms are in blue and O in red. Scale bar, 5 Å. (C)-(D) Electric-field maps calculated from the 4D-STEM dataset collected from the black boxed areas in (A) and (B), respectively. The vector arrows represent the direction and magnitude of the local electric field (in volts). (E)-(F) Charge density maps reconstructed from the 4D-STEM dataset collected from the red boxed areas in (A) and (B), respectively. The red arrow below indicates the direction of polarization and the "X" means nonpolarized. (G)-(H) Total and ionic polarization of ZrO_2 in polar O-phase (G) and nonpolar T-phase (H) calculated from experimental data.

based on PBE exchange correlation function at GGA theoretical level and 8 × 8 × 8 k-point mesh and 800 eV energy cutoff are used. The difference charge density is calculated by subtracting charge densities of both Zr and O ions from total charge density. We calculate charge densities of Zr and O ions respectively by moving out another kind of ions but holding on the shape of unit cell and the position of each atom. Matrix element of born effective charge is calculated according to following expression[27]

$$q_{zz} = \frac{\Omega}{e}\frac{\delta P_z}{\delta d_z}$$

where Ω is the unit cell volume, e is elementary charge, δP_z is the change of total polarization, namely the summation of ionic and electronic polarization, along z-axis and δd_z is a tiny shift along z-axis.

We also calculate the ferroelectric polarization by DFT. In order to obtain a reasonable structure of non-polar reference phase, we build two ferroelectric cell of O-phase ZrO_2 with opposite polarization along z-axis and apply the nudged elastic band (NEB) method implemented in the VASP with Vasp Transition State Theory Tools (VTST Tools) for structure interpolation as well as phase transition path optimization. We calculate the polarization of each optimized interpolation structure from non-polar reference phase to ferroelectric O-phase via VASP based on Berry phase expression in modern theory of polarization. Linear fitting is used to solve the multivalued problem of polarization in periodic systems. Finally, we rescale the spontaneous polarization value to match with the calculation method in the experiment. At last, the total polarization in the polar subcell is 114.78 $\mu C/cm^2$ by DFT calculation. This result is closer to our experimental value (123.45 $\mu C/cm^2$).

RESULTS AND DISCUSSION

Figure 1A shows a diagram of the 4D-STEM geometry used, where the highspeed pixelated detector is used to capture convergent beam electron diffraction (CBED) patterns at each scan position (Figure 1D) in real-space. Different probe positions show variations in the CBED patterns (Figures 1D–F). According to previous research, the center of mass (COM) of the CBED intensity distribution is shifted by interatomic forces including atomic electric field and local magnetic field.[28] The projection average of electric field along the electron beam direction (E_{xy}) is proportional to the expected value of the momentum transfer, which can be measured from the shift in the COM from the geometric center in milliradians ΔCOM).[29] Based on the Gauss's law, the projected charge density ρ_{xy} can be obtained by the divergence of E_{xy}. The atomic structure of FE O-phase obtained from density functional theory (DFT) calculations shown in Figure 1B can only be achieved in ZrO_2 thin films with a thickness below 10 nm,[30] absence in bulk ZrO_2. One peculiar feature of the O phase atomic structure is that polar and nonpolar O columns are unequally spaced by Zr columns when viewed in the [100] projection direction. Besides, the polarized O columns are located at the off-center sites, constituting localized electric dipoles within polar Zr-O layers. In contrast, Figure 1C depicts the atomic structure of the nonpolar tetragonal phase (T-phase), where the Zr columns are equally spaced and the unpolarized O columns are located at the center of the nearest Zr ions in the [100] projection.

We firstly compare the charge distribution and polarization configuration between ferroelectric orthorhombic and non-ferroelectric tetragonal ZrO_2. Figure 2A displays the high angle annular dark field (HAADF) image reconstructed from 4D-STEM dataset. It can be inferred from the unequal distance between Zr columns that the corresponding specimen is FE O-phase, although the O columns are invisible due to the insensitivity of the light elements of the HAADF imaging technique. Based on the principle shown in Figure 1A, the projected electric field E_{xy} is extracted and shown in Figure 2C. The electric field surrounding the Zr columns is no longer radially symmetric: the field is weak at the top left and stronger at the bottom right across the Zr site. The strength of the electric field increases sharply in the vicinity of Zr sites, in accordance with Coulomb's law. However, the field strength decreases in the vicinity of nuclei and reaches a minimum in the center of an atomic position due to the finite size of the scanning transmission electron microscopy (STEM) probe. In other words, the measured electric field is actually a convolution of the true electric field with the normalized probe intensity.[31]

A 2D projection image of the local charge density can be constructed from the corresponding electric-field landscape via Gauss's law. Figures 2E-F display 2D charge density images of O- and T-phase ZrO_2 projected along the [100] zone axis. The projected charge density maps contain contributions from both the electron charge densities and the atomic nuclei convolved with the probe intensity. It should be noted that the nuclear charge distributions spread as broad Gaussians as a result of the shielding effect of the core electrons and the finite size of the electron probe. The atomic sites have a net

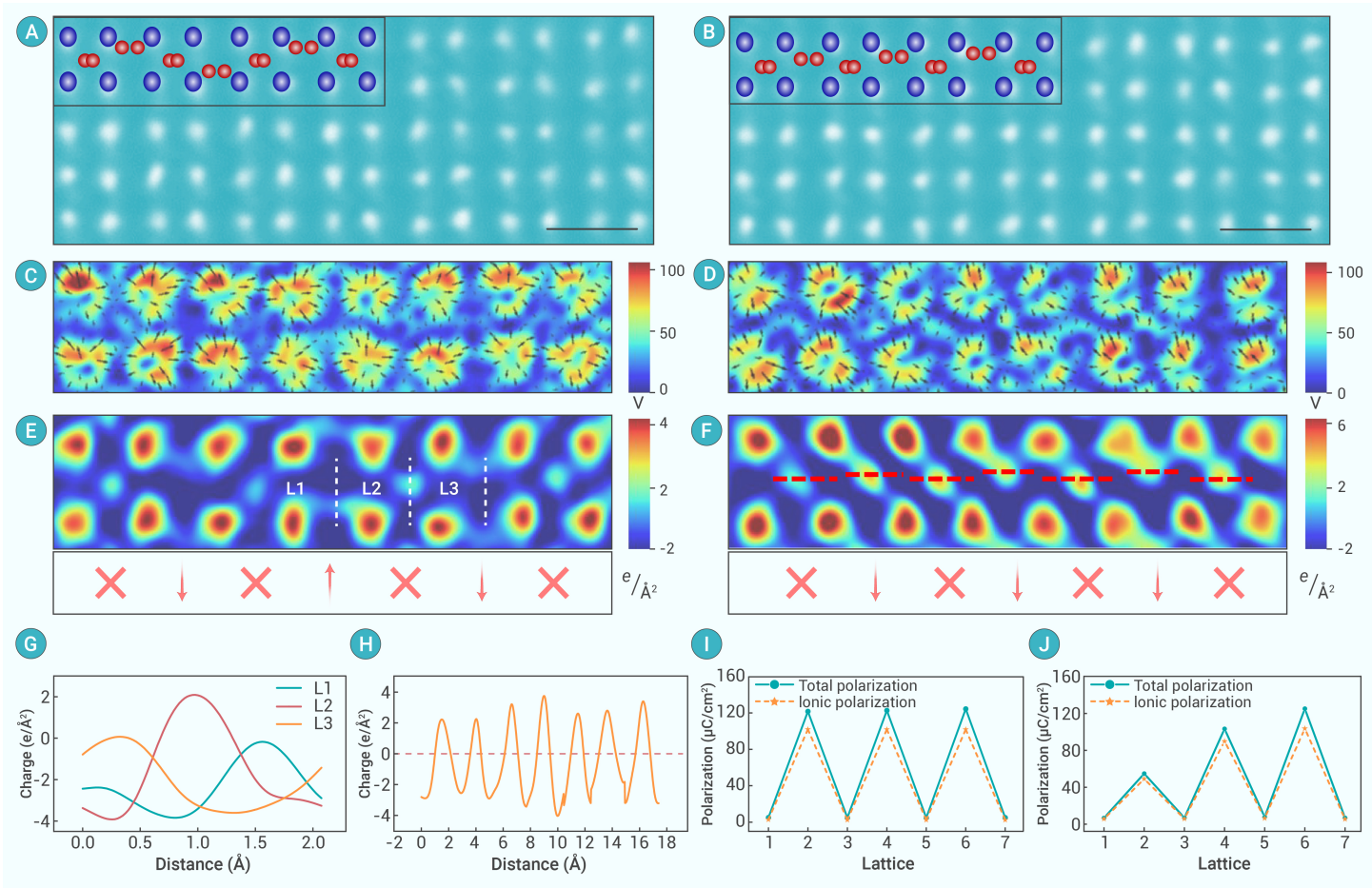

Figure 3. Charge-density and polarization in polar-antipolar fixed state and the T-O phase interface (A)-(B) Atomic-resolved HAADF images in the polar-antipolar fixed phase (A) and at the T-O phase interface (B) taken from the [100] zone axis. Zr atoms are in blue and O in red. Scale bar, 5 Å. (C)-(D) Corresponding electric-field maps calculated from the 4D-STEM dataset collected from the red boxed areas in (A) and (B), respectively. (E)-(F) Corresponding charge density maps reconstructed from the 4D-STEM dataset collected from the black boxed areas in (A) and (B), respectively. The red arrow below indicates the direction of polarization and the "X" means nonpolarized. (G) Line profiles (L1 to L3 from left to right) taken along the white dotted lines in (E), from top to bottom. (H) Line profile taken along the red dotted lines in (F), from left to right. (I)-(J) Total and ionic polarization of ZrO_2 (I) in the polar-antipolar mixed phase and (J) at the T-O phase interface calculated from experimental data.

positive charge (red) indicating a higher contribution from the atomic nucleus, while the regions around the atomic sites have a net negative charge (blue) for a higher contribution from the electrons. An obvious result of such charge density mapping is the distinct appearance of the O atomic columns regardless of polar or nonpolar phases, which is of great advantage over HAADF or electric field images for O atoms localization. It can be seen from Figure 2E that for the nonpolar layer, the charge density projections of two adjacent O columns overlap and appear almost as a circle, slightly stretching in the diagonal direction. In sharp contrast, the two O columns in the polar layer overlap and appear as an ellipse with a slight diffusion into the surroundings in the 2D projection. Since structural stability is related to the electronic structure and chemical bonding, the results reveal the key role of oxygen sites in the reliability of FE ZrO_2 films.[31,32]

Besides, a clear separation of the positive and negative charge center can be seen in the polar layer, and a net dipole moment pointing downwards indicated by the red arrow is clearly revealed (Figure 2E). This result is in agreement with the calculated polarization in Figure 2G, where the total polarization appears to be larger than the ionic polarization, especially for the polar layer. The ionic polarization P_i of each layer was calculated using the point charge model, [6,7,33]

$$P_i = \frac{1}{V_{subcell}} 4e \cdot l$$

Where the $V_{subcell}$ is calculated as a_{m*} b_{m*} c_m and a_m =5.32 Å is the theory lattice constant along the beam direction, b_m and c_m are the length and width of the marked rectangle shown in Figure S5. The origin of the coordinate is the center of the rectangle in each subcell. Besides, e and l are the elementary charge and vertical displacement from the center of the O atom columns to the origin, respectively. The approach to define l is also illustrated in Figure S5. The total spontaneous polarization P_s was calculated locally by summing the dipole moment of each pixel in the defined subcell as follows:[6,7,33]

$$P_s = \frac{1}{V_{subcell}} \sum_j \rho_j \Delta r_j$$

Where the $V_{subcell}$ is calculated as a_{p*} b_{p*} c_p and a_p =5.32 Å is the theory lattice constant along the beam direction, b_p and c_p are the length and width of the marked rectangle shown in Figure S6. The origin of the coordinate is the center of the rectangle in each subcell and $\rho_j, \Delta r_j$ are the charge density of each pixel obtained from the 4D dataset and vertical distance from the corresponding pixel position to the origin, respectively.

Since the contribution of both ionic and electronic polarizations should be considered in the calculation of the spontaneous polarization, the difference between the total polarization and the ionic polarization represents the electronic polarization, which accounts for approximately 17% of the spontaneous polarization in the polar layer of the O-phase. Projected density of states (PDOS) in Figure 4A obtained via DFT-GGA calculation shows demonstrable overlap between O-2p and Zr-4d orbitals in both valence and condition bands. Ulteriorly, more details about the occupation at different K points in valance band, namely within ranges from -5 eV to 0 eV, are shown in Figure 4B. The results indicate considerable hybridization between orbitals of neighboring Zr and O ions, and the aberrations of electronic clouds accompanied with such hybridization maybe vital origin of the considerable electronic polarization.[4,6,7,34,35]

Compared with Figure 2C, Figure 2D displays a relatively centrosymmetric

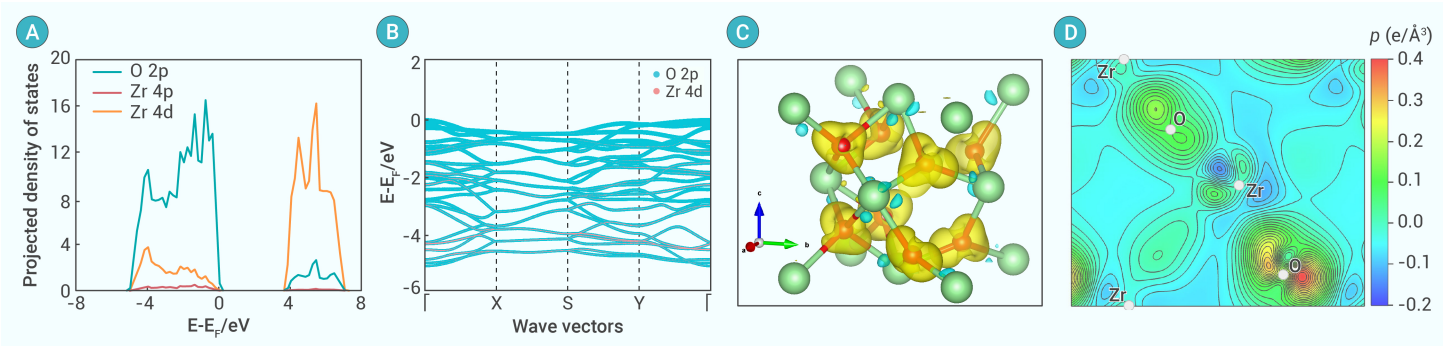

Figure 4. DFT calculation results of ZrO_2 in the O-phase (A) Projected density of state for ZrO_2. (B) Projected band structure. Blue and red dots correspond to O-2p and Zr-4d orbitals, respectively, while radius of each dot represents the contribution of a single orbital at a certain energy level and a certain k-point. (C) Deformation Charge density ($\rho_{model} - \rho_{IAM}$) and (D) 2D slice along [100] zone axis. The lowest contour shown is −0.2 e/Å^3. The highest contour shown is 0.4 e/Å^3. The contour level is 0.02 e/Å^3.

electric field, consistent with the crystallographic symmetry of the nonpolar T-phase. Furthermore, the projected charge density of ZrO_2 in T-phase shows a four-fold symmetry around the columns of Zr atoms, with the O atom column located at the center of the square formed by the four Zr columns. This indicates that the O atom columns in the T-phase are centrosymmetric at the local atomic scale. Meanwhile, the corresponding polarization profile shown in Figure 2H is close to a horizontal line with a value close to zero. The small fluctuation around 0.7 $\mu C/cm^2$ is probably due to experimental limitations such as specimen drift and scan noise. In conclusion, the O atom columns in the T-phase are not polarized regardless of the micro-local or macro-average level.

It is also worth noting that the observed FE polar and antipolar mixed phase is much more abundant than the pure polar phase in the ZrO_2 thin film (Figure S4). We enlarged a polar-antipolar mixed region to make the comparison with the pure polar phase accordingly, as shown in Figure 3C, which corresponds to a 'nonpolar-polar-nonpolar-antipolar-nonpolar-polar-nonpolar' configuration. An obvious difference is that the electric field around the O columns between the polar and antipolar layers is relatively more radially symmetric than that in the pure antipolar phase. Meanwhile, the length of the vector arrow is shorter around the O columns, which means that the magnitude of the electric field is closer to zero. It can be inferred from the above experimental phenomenon that the nonpolar layer between polar and antipolar layers acts as an isolation layer, which can partially block the penetration of electric field from the polar layer to the antipolar layer.

The local charge density map of typical polar-antipolar mixed phase is shown in Figure 3E. The upward electric dipole is particularly evident in the charge density distribution near the O columns in the antipolar layer. To compare the polarization value between the polar and antipolar layer, we calculate the absolute value of total and ionic polarization (Figure 3I). It is evident from Figure 3I that there is a separation of electronic polarization between the antipolar and polar layers by the nonpolar spacer layers. Additionally, the line profiles for charge density in Figure 3G exhibit almost symmetrical behavior along the vertical "Distance=1 Å" line. This indicates that the charge density distribution around the off-center O columns in the polar and antipolar layer is centrosymmetric with respect to the central O columns in the nonpolar layer. Contrary to conventional ferroelectrics, whose spread dipoles fade away below critical nano-dimensions,[36–38] the dipoles in this case, particularly the electronic contributions, remain localized. This characteristic facilitates the retention of a stable and switchable ferroelectric phase even at the sub-nanometer scale.

In contrast with Figures 2C-D, the electric field image at the T-O phase interface displays apparently deformed shapes in the vicinity of the Zr columns. As shown in Figure 3D the field is weak on the right side and stronger on the left side across the Zr site. Meanwhile, the 2D charge-density near the Zr columns exhibits elliptical geometry, which might originate from the O atoms shifting away from the principal axis and orbital exchange interactions at the phase interface.[5] The presence of more intense green pockets between the O atom and the lower left Zr atom near the T-O phase interface indicates the transitional increasing covalent nature of Zr-O bond. This is also supported by analysis of the charge density line profile (Figure 3H) and polarization (Figure 3J). The charge density lines show an interesting evolution that O atom is surrounded by more regions of negative charge, indicating more shared electrons between the O site and Zr atoms from T-phase to O-phase. Based on the DFT calculations presented in Figure 4, there may be considerable hybridization between orbitals of neighboring Zr and O ions in the O-phase. This is particularly significant as it governs several physical and chemical properties in ferroelectric materials.[30,34,39,40] According to Figure 3J, the calculated polarization values in each sublayer from left to right correspond to a "nonpolar-polar" alternating atomic structure. However, the second calculated polarization value reaches 58 $\mu C/cm^2$, which is less than half of the sixth polarization value, showing an intermediate state between polar and nonpolar. Furthermore, the electronic polarization becomes larger as ZrO_2 transitions from T-phase to O-phase, which is consistent with our 4D-STEM simulation results (Figure S17). These results further confirm the hypothesis that electronic polarization is closely connected to the origin of ferroelectricity in ZrO_2.

To visually show that the redistribution of electrons in real space results from the overlap of Zr and O orbitals, we calculate the differential charge density, named as deformation charge density (ρ_{def}), within a periodic unit cell via DFT at the theoretical level of generalized gradient approximation (GGA). The deformation charge density is calculated as:

$$\rho_{def} = \rho_{model} - \rho_{IAM}$$

where ρ_{model} is the total charge density and ρ_{IAM} is the charge density calculated from independent atom model (IAM). In the IAM, each atom, called a pseudoatom, is assumed to be spherical and the density is inert to the chemical surroundings. Isosurface of ρ_{def} in Figure 4C shows obvious deformation of charge density between Zr atoms and O atoms, further confirming the hybrid of O-2p orbitals and Zr-4d orbitals. Furthermore, cross section in Figure 4D clearly reveals that Zr atoms share more electrons with polar O atoms than nonpolar ones, which is consistent with the results in Figure 2E. Besides, the matrix element of Born effective charge q_{zz} shown in Figure S9 indicates that, comparing with that in T-phase , each O atom get closer to some of the neighboring Zr stoms, which could result in stronger locally orbital overlap and more significant electronic polarization. This result is also consistent with the electronic polarization difference in Figure 3J.

It is noteworthy that the performance of films with electrodes may be affected by the complicated electrode-film interactions. In our study, we exclude such effects and focus on the intrinsic properties of fluorite oxides by investigating ZrO_2 freestanding films (Figure S8). In this work, the observed local charge density map and correlated electronic polarization values are inherent to the fluorite crystal structure. Moreover, this work could provide a fundamental understanding of the underlying mechanisms in the fluorite-oxide devices.

CONCLUSION

In summary, we have mapped the local charge density of ZrO_2 thin film in the (non)polar phases in real space with sub-Ångström resolution 4D-STEM and calculated the local ionic and electronic polarization in the atomic scale. The significant difference in electric field and charge density between polar and nonpolar layers is revealed, indicating the anisotropic interactions between O-2p and Zr-4d orbitals. Meanwhile, we have also demonstrated the

atomic-scale charge density distribution at the interface of O-phase and T-phase, as well as the variation in electric dipole moments and polarization in the interfacial region. The gradual increase in the magnitude of the electronic polarization implies the increasing covalent nature of the Zr-O bond from nonpolar T-phase to polar O-phase. The results indicate that the origin of stable ferroelectric O-phase might connect with the local electronic interaction between O-2p state and Zr-4d state. The ability to experimentally reveal electron redistribution and to calculate local electronic polarization in fluorite oxides at the subatomic level may open a new perspective, providing a fundamental basis for regulating the properties of ferroelectric materials and designing new functional materials.

REFERENCES

1. Valasek, J. (1921). Piezo-electric and allied phenomena in rochelle salt. Phys. Rev. **17**: 475–481. DOI: 10.1103/PhysRev.17.475.
2. Kittel, C. (1951). Theory of antiferroelectric crystals. Phys. Rev. **82**: 729–732. DOI: 10.1103/PhysRev.82.729.
3. Jaffe, B. (1961). Antiferroelectric ceramics with field-enforced transitions-new nonlinear circuit element. Proc. Inst. Radio. Eng. **49**: 1264–1270. DOI: 10.1109/JRPROC.1961.287917.
4. Cohen, R. (1992). Origin of ferroelectricity in perovskite oxides. Nature **358**: 136–138. DOI: 10.1038/358136a0.
5. Dash, L., Vast, N., Baranek, P.,et al. (2004). Electronic structure and electron energy-loss spectroscopy of ZrO_2 zirconia. Phys. Rev. B **70**: 245116. DOI: 10.1103/PhysRevB.70.245116.
6. Abe, T., Kim, S., Moriyoshi, C., et al. (2020). Visualization of spontaneous electronic polarization in Pb ion of ferroelectric $PbTiO_3$ by synchrotron-radiation X-Ray diffraction. Appl. Phys. Lett. **117**: 252905. DOI: 10.1063/5.0037396.
7. Kawamura, S., Magome, E., Moriyoshi, C.,et al. (2013). Electronic polarization in $KNbO_3$ visualized by synchrotron radiation powder diffraction. Jpn. J. Appl. Phys. **52**(9S1): 09KF04. DOI: 10.7567/JJAP.52.09KF04.
8. Boescke, T., Muller, J., Brauhaus, D., et al. (2011). Ferroelectricity in hafnium oxide thin films. Appl. Phys. Lett. **99**: 102903. DOI: 10.1063/1.3636417.
9. Muller, J., Boscke, T., Brauhaus, D., et al. (2011). Ferroelectric $Zr_{0.5}Hf_{0.5}O_2$ thin films for nonvolatile memory applications. Appl. Phys. Lett. **99**: 112901. DOI: 10.1063/1.3636417.
10. Fan, Z., Deng, J., Wang, J.,et al. (2016). Ferroelectricity emerging in strained (111)-textured ZrO_2 thin films. Appl. Phys. Lett. **108**: 012906. DOI: 10.1063/1.4939660.
11. Mueller, J., Boescke, T.S., Schroeder, U., et al. (2012). Ferroelectricity in simple binary ZrO_2 and HfO_2. Nano Lett. **12**: 4318–4323. DOI: 10.1021/nl302049k.
12. Huan, T., Sharma, V., Rossetti, G., et al. (2014). Pathways towards ferroelectricity in hafnia. Phys. Rev. B **90**: 064111. DOI: 10.1103/PhysRevB.90.064111.
13. Schroeder, U., Park, M.H., Mikolajick, T., et al. (2022). The fundamentals and applications of ferroelectric HfO_2. Nat. Rev. Mater. **7**: 653–669. DOI: 10.1038/s41578-022-00431-2.
14. Cheema, S.S., Shanker, N., Wang, L.-C., et al. (2022). Ultrathin ferroic HfO_2-ZrO_2 superlattice gate stack for advanced transistors. Nature **604**: 65–72. DOI: 10.1038/s41586-022-04425-6.
15. Cheema, S.S., Shanker, N., Hsu, S.-L., et al. (2022). Emergent ferroelectricity in subnanometer binary oxide films on silicon. Science **376**: 648–653. DOI: 10.1126/science.abm8642.
16. Clima, S., Wouters, D.J., Adelmann, C., et al. (2014). Identification of the ferroelectric switching process and dopant-dependent switching properties in orthorhombic HfO_2: A first principles insight. Appl Phys Lett **104**: 092906. DOI: 10.1063/1.4867975.
17. Rushchanskii, K., Blugel, S., and Lezaic, M. (2021). Ordering of oxygen vacancies and related ferroelectric properties in HfO_2.delta. Phys. Rev. Lett. **127**: 087602. DOI: 10.1103/PhysRevLett.127.087602.
18. Grimley, E.D., Schenk, T., Mikolajick, T., et al. (2018). Atomic structure of domain and interphase boundaries in ferroelectric HfO_2. Adv. Mater. Interfaces **5**: 1701258. DOI: 10.1002/admi.201701258.
19. Ding, W., Zhang, Y., Tao, L.,et al. (2020). The atomic-scale domain wall structure and motion in HfO_2-based ferroelectrics: A first-principle study. Acta Mater. **196**: 556–564. DOI: 10.1016/j.actamat.2020.07.012.
20. Hsain, H.A., Lee, Y., Lancaster, S., et al. (2022). Role of oxygen source on buried interfaces in atomic-layer-deposited ferroelectric hafnia-zirconia thin films. ACS Appl. Mater. Interfaces **2**: 10.1021. DOI: 10.1021/acsami.2c11073.
21. Yi, S., Lin, B., Hsu, T.,et al. (2019). Modulation of ferroelectricity and antiferroelectricity of nanoscale ZrO_2 thin films using ultrathin interfacial layers. J. Eur. Ceram. Soc. **39**: 4038–4045. DOI: 10.1016/j.jeurceramsoc.2019.05.065.
22. Gao, W., Addiego, C., Wang, H., et al. (2019). Real-space charge-density imaging with sub-ångström resolution by four-dimensional electron microscopy. Nature **575**: 480–484. DOI: 10.1038/s41586-019-1649-6.
23. Fang, S., Wen, Y., Allen, C.S., et al. (2019). Atomic electrostatic maps of 1D channels in 2D semiconductors using 4D scanning transmission electron microscopy. Nat. Commun. **10**: 1127. DOI: 10.1038/s41467-019-08904-9.
24. Ophus, C. (2019). Four-dimensional scanning transmission electron microscopy (4D-STEM): From scanning nanodiffraction to ptychography and beyond. Microsc. Microanal. **25**: 563–582. DOI: 10.1017/S1431927619000497.
25. Lin, R., Zhang, R., Wang, C., et al. (2021). TEMimageNet training library and AtomSegNet deep-learning models for high-precision atom segmentation, localization, denoising, and deblurring of atomic-resolution images. Sci. Rep. **11**: 386. DOI: 10.1038/s41598-021-84499-w.
26. Muellller-Caspary, K., Krause, F.F., Grieb, T., et al. (2017). Measurement of atomic electric fields and charge densities from average momentum transfers using scanning transmission electron microscopy. Ultramicroscopy **178**: 62–80. DOI: 10.1016/j.ultramic.2016.05.004.
27. Spaldin, N. (2012). A beginner's guide to the modern theory of polarization. J. Solid State Chem. **195**: 2–10. DOI: 10.1016/j.jssc.2012.05.010.
28. Caswell, T.A., Ercius, P., Tate, M.W., et al. (2009). A high-speed area detector for novel imaging techniques in a scanning transmission electron microscope. Ultramicroscopy **109**: 304–311. DOI: 10.1016/j.ultramic.2008.11.023.
29. Mueller, K., Krause, F.F., Beche, A., et al. (2014). Atomic electric fields revealed by a quantum mechanical approach to electron picodiffraction. Nat. Commun. **5**: 5653. DOI: 10.1038/ncomms6653.
30. Polakowski, P., and Muller, J. (2015). Ferroelectricity in undoped hafnium oxide. Appl. Phys. Lett. **106**: 232905. DOI: 10.1063/1.4922272.
31. Lazić, I., Bosch, E.G.T., and Lazar, S. (2016). Phase contrast STEM for thin samples: integrated differential phase contrast. Ultramicroscopy **160**: 265–280. DOI: 10.1016/j.ultramic.2015.10.011.
32. Mittmann, T., Materano, M., Chang, S.-C.,et al (2020). Impact of oxygen vacancy content in ferroelectric HZO films on the device performance. IEEE Inter Electron Devices Meet **1**: 973209. DOI: 10.1109/IEDM13553.2020.9372097.
33. Nelson, C., Winchester, B., Zhang, Y.,et al. (2011). Spontaneous vortex nanodomain arrays at ferroelectric heterointerfaces. Nano Lett. **11**: 828–834. DOI: 10.1021/nl1041808.
34. Pan, Y. (2019). Influence of oxygen vacancies on the electronic and optical properties of zirconium dioxide from first-principles calculations. J. Electron. Mater. **48**: 5154–5160. DOI: 10.1007/s11664-019-07325-0.
35. Cohen, R., and krakauer, H. (1990). Lattice-dynamics and origin of ferroelectricity in $BaTiO_3$-linearized-augmented-plane-wave total-energy calculations. Phys. Rev. B **42**: 6416–6423. DOI: 10.1103/PhysRevB.42.6416.
36. Chu, M., Szafraniak, I., Scholz, R., et al. (2004). Impact of misfit dislocations on the polarization instability of epitaxial nanostructured ferroelectric perovskites. Nat. Mater. **3**: 87–90. DOI: 10.1038/nmat1057.
37. Ihlefeld, J.F., Harris, D.T., Keech, R., et al. (2016). Scaling effects in perovskite ferroelectrics: fundamental limits and process-structure-property relations. J. Am. Ceram. Soc. **99**: 2537–2557. DOI: 10.1111/jace.14387.
38. Wang, Y., Zhong, W., and Zhang, P. (1995). Lateral size effects on cells in ferroelectric-films. Phys. Rev. B **51**: 17235–17238. DOI: 10.1103/PhysRevB.51.17235.
39. Eastman, J.A. (2022). Another route to ferroelectric HfO_2. Nat. Mater. **21**: 845–847. DOI: 10.1038/s41563-022-01297-z.
40. Cheng, Y., Gao, Z., Ye, K., et al. (2022). Reversible transition between the polar and antipolar phases and its implications for wake-up and fatigue in HfO_2-based ferroelectric thin film. Nat. Commun. **13**: 645. DOI: 10.1038/s41467-022-28236-5.

FUNDING AND ACKNOWLEDGMENTS

This work was financially supported by the National Natural Science Foundation of China (52250402, 52322212, 52072400, 52025025 and 51991344) and the National Key R&D Program of China (2019YFA0308500). The funders had no role in study design, data collection and analysis, decision to publish or preparation of the manuscript.

AUTHOR CONTRIBUTIONS

L.G. conceived of the study. S.Y.W. processed raw data. Y.Z.J performed theoretical computations. H.Z. and H.X. synthesized the samples. Q.H.Z, P.X.J, and X.C. performed experiments and collected data. S.Y.W wrote and revised the manuscript. L.G. and Q.H.Z supervised the project, and all authors contributed to writing and editing the document.

DECLARATION OF INTERESTS

Lin Gu is an Editorial Board member of The Innovation Materials and was blinded from reviewing or making final decisions on the manuscript. Peer review was handled independently of this member and their research group. The other authors declare no conflicts of interest.

DATA AND CODE AVAILABILITY

All data and code are available from the corresponding authors upon reasonable request.

SUPPLEMENTAL INFORMATION

It can be found online at https://doi.org/10.59717/j.xinn-mater.2024.100068